IEEE Access
Multidisciplinary ⋮ Rapid Review ⋮ Open Access Journal

Received 13 April 2024, accepted 23 April 2024, date of publication 29 April 2024, date of current version 6 May 2024.

Digital Object Identifier 10.1109/ACCESS.2024.3395121

RESEARCH ARTICLE

Open-Circuit Fault Diagnosis for a Modular Multilevel Converter Based on Hybrid Machine Learning

YANG AN, XIANGDONG SUN, (Member, IEEE), BIYING REN, AND XIAOBIN ZHANG, (Member, IEEE)
School of Electrical Engineering, Xi'an University of Technology, Xi'an 710054, China
Corresponding author: Xiangdong Sun (sxd1030@xaut.edu.cn)

This work was supported in part by the Natural Science Foundation of Shaanxi under Grant 2023-JC-YB-390, and in part by the Natural Science Basic Research Program Foundation of Shaanxi under Grant 2022JM-288.

ABSTRACT With the wide application of a modular multilevel converter in various power conversion fields, submodule open-circuit fault diagnostics have attracted increasing attention, as some of the existing diagnosis methods have a single function and limited localization speed. Therefore, a simplified and innovative multifunctional hybrid machine learning-based fault diagnosis strategy for the submodules is proposed. Starting from the output characteristics of the faulty submodule, the eigenvalues of the bridge arm current and submodule capacitor voltage during faults are extracted, and the eigenvalues are utilized for fault detection and location via the integration of improved supervised learning and unsupervised learning. Finally, the effectiveness of the proposed method is verified by simulated and experimental results in a three-phase modular multilevel converter topology. In addition, it can diagnose multiple fault types and achieve a high fault identification probability.

INDEX TERMS Artificial neural networks, data processing, fault diagnosis, fault detection, fault location, multilevel converters, machine learning, power conversion, supervised learning, unsupervised learning.

I. INTRODUCTION

Modular multilevel converters (MMCs) are becoming popular circuit topologies in HVDC applications [1], [2], [3], where they offer the advantages of high flexibility, flexible changes in voltage and power levels, and lower switching frequency and power loss. Therefore, MMCs are widely used in the fields of energy storage [4], [5], microgrids [6], [7], power electronic transformers [8], [9], renewable power generation [10], motor drive [11], rail transport [12], and flexible DC transmission [13], [14]. Compared with other power electronic converters, the submodule (SM) faults are the main factor affecting the reliability of the MMCs [15]. These faults include wiring failure, capacitor failure, semiconductor device failure and other failures (as shown in Figure 1).

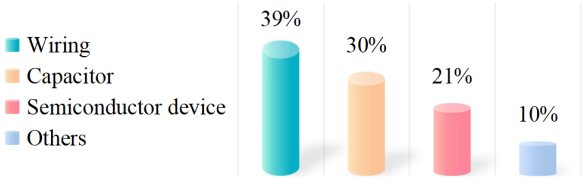

FIGURE 1. Probability of submodules with different fault types. While 39% of the faults may be wiring faults, 30% may be capacitor faults, 21% may be semiconductor device failures, and 10% may be other faults.

Moreover, the fault probability of the MMC increases with the number of SMs.

Generally, power electronic device faults include short-circuit faults and open-circuit faults. The former can cause overcurrent and damage the circuit. Thus, gate drivers are typically integrated with short-circuit protection functions to protect devices immediately when a short-circuit fault

The associate editor coordinating the review of this manuscript and approving it for publication was Gerard-Andre Capolino.

is detected [16], [17]. In contrast, the latter is difficult to detect in a timely manner [18] and can overcharge capacitors [19] and deteriorate the system output quality [20]. For a high-capacity MMC system, a wire-bonding IGBT module can be connected in parallel to form the MMC system. Under such conditions if an SM is in a prolonged short-circuit state, the SM can easily turn into an open-circuit fault. Therefore, SM open-circuit faults are an urgent problem that need to be solved in MMCs. In this context, open-circuit fault detection and location (OCFDL) of SMs is beneficial for improving the reliability of MMCs. Thus, OCFDL is the main topic of this paper.

OCFDL methods for MMCs have been extensively studied in previous works. However, there are few reports on multifunctional hybrid fault diagnosis models in which SM fault locations do not need to collect fault samples data. At present, these fault diagnosis methods can be divided into three main categories: hardware-based, model-based and AI-based methods. For hardware methods, a hardware detection circuit was designed for fault detection in [21]. However, only unitary SM open-circuit faults can be diagnosed via this method, and multiple SM open-circuit faults cannot be identified. A fault detection, localization, redundancy and recovery strategy was proposed in [22], which requires limited hardware and software resources. Nevertheless, with the increase in the number of SMs in an MMC system, this approach would be suitable for applications in high voltage fields due to its high cost and increased circuit complexity. In [23], a method for detecting IGBTs in an open-circuit fault is proposed for each grouping detection device, which consists of two submodules and a voltage sensor. This method has a high-speed fault detection advantage, however, it cannot achieve SM fault location fuctionality. Regarding model-based methods [24], [25], [26], [27], [28], solutions for fault diagnosis have been developed. In [24], a multipoint SM fault diagnosis strategy under a low modulation index was proposed, which improves upon the existing sliding-mode observer and achieves rapid location of the faulty arm. In [25], a concurrent and direct fault diagnosis method was been proposed by comparing the measured and estimated values using an amending Kalman filter. Nevertheless, the above two methods are not suitable for applications in high-voltage fields due to their high-accuracy model and algorithm complexity. A grouping capacitor voltage estimation method with capacitance self-updating was designed for OCFDLs [26], and at least a few sampling cycles are required to identify the severe aging or faulty capacitors used in MMCs. A fast and simple OCFDL scheme was proposed by analyzing the similarity of capacitor voltages under both normal and fault conditions [27]. However, [26] and [27] need a longer capacitor voltage charging process, which increases the cost of the fault diagnosis time. In [28], a threshold adaptive diagnosis strategy was proposed in which the fault is diagnosed by determining whether the SM capacitor voltage exceeds the threshold. Nevertheless, this method is not equipped with a diagnostic function for multiple open-circuit faults.

The most popular fault diagnosis methods are mainly AI-based methods. An open-circuit fault diagnosis method based on extreme gradient boosting is proposed [29], [30], which has excellent robustness against external noise with an accuracy as high as 99.2% within 20 ms. Because this method adopts a nonparallel structure, the occurrence of multiple SM faults is not perfectly resolved. A two-dimensional trajectory pattern-based fault detection method for SMs was proposed in [31]. Kiranyaz et al. [32] presented real-time fault detection and identification methods for MMCs using 1D convolutional neural networks, which achieved an average identification probability of 0.9993 in less than 100 ms. Bai et al. [33] presented a dual 1D CNN diagnosis and recognition method based on the sub-unit voltage and bridge arm current. However, the above three methods can increase the computational burden by training on many fault samples. Ke et al. [34] proposed a novel multimodal attention fusion (MAF) model in which the fault diagnosis accuracy of the proposed model was 98.4%. However, this method has poor generalizability and robustness and is sensitive to system changes caused by environmental noise. In [35], a novel fault diagnosis method based on shorttime wavelet entropy integrating a long short-term memory network (LSTM) and a support vector machine (SVM) was proposed, where only the bridge arm current signal was used as the sampling signal. However, this method does not mention the fault location of the SM. In addition, many electrical signal samples should be trained. Ke et al. [36] proposed a compound fault diagnosis method based on an improved capsule network. Tong et al. [37] proposed a methodology to deploy a DNN with fault diagnosis purpose at the edge. Wang et al. [38] proposed a machine learning-based fault self-test, which can quickly determine the fault item in time and reduce the maintenance cost later. However, [36], [37], and [38] have obvious drawbacks that are not applicable to multiple SM open-circuit faults and increase the time cost of sample training.

In summary, these existing OCFDL methods involve completing fault diagnosis within the desired index. Nevertheless, hardware-based and model-based methods for fault diagnosis usually have limited localization speeds or are difficult to apply in practical systems. Furthermore, the conventional machine learning-based fault diagnosis methods have a single diagnostic function or require considerable time for training fault samples. Faced with the large number of SMs in actual MMC systems, a new strategy urgently needs to address the issues of a single diagnosis function or the high time cost of training samples. Therefore, an innovative OCFDL method for MMCs based on hybrid machine learning is proposed in this article. This method has multiple diagnostic functions and reduces the time cost of diagnosis. In other words, the proposed method can locate multiple faults effectively without training fault samples, which is more suitable for enormous MMC systems.

To address the above challenges, we leverage the hybrid machine learning scheme for MMC fault diagnosis, which integrates the supervised learning of a long short-term memory (LSTM) neural network and the unsupervised learning of K-means. The main contributions of this paper are highlighted as follows:

1) The proposed method can determine the fault location without training fault samples, and a single faulty SM or multiple faulty SMs can be localized within 10 ms.
2) The hybrid machine learning model does not require accurate mathematical models or additional sensors.
3) An improved LSTM neural network was constructed by the quantum particle swarm optimization (QPSO) algorithm for SM open-circuit fault detection.
4) To cluster data more conveniently, an improved K-means method is implemented by defining an evaluation function, which reduces the dependence on manual values.
5) A hybrid machine learning model is designed by the integrating supervised learning and unsupervised learning.

The remainder of this paper is organized as follows: Section II briefly introduces the SM open-circuit fault analysis of MMCs. In Section III, the supervised and unsupervised hybrid machine learning methods are presented. The simulation and experimental verification and analysis are performed in Sections IV and V, respectively. Conclusions are drawn in Section VI.

II. ANALYSIS OF SM OPENCIRCUIT FAULTS FOR MMCs

A. MMC TOPOLOGY

An MMC comprises many SMs with the same structure. Considering each bridge arm with 4 SMs, the structure of the three-phase MMC is shown in Figure 2. Each phase in a three-phase MMC circuit topology is divided into upper and lower arms, and each arm consists of N identical SMs and a bridge arm inductance L_0. The SM is a typical half-bridge structure that includes a DC capacitor, two IGBT devices (T1 and T2) and two antiparallel diodes (D1 and D2). U_{dc} is the DC-link voltage, U_{SM} is the output voltage across the SM, and C is the SM capacitance. Because there are many switching devices in the MMC system, if an open-circuit fault occurs during SM operation, then the output voltage and bridge arm current of the system will be distorted. To extract fault features, it is therefore necessary to analyze the principle of various faults for SMs.

B. SM OPEN-CIRCUIT FAULT ANALYSIS

Typically, T1 and T2 in a half-bridge SM work in a complementary manner. The working state S of the SM is defined as follows:

$$S = \begin{cases} 1, & \text{T1 turns on and T2 turns off} \\ 0, & \text{T1 turns off and T2 turns on} \end{cases} \quad (1)$$

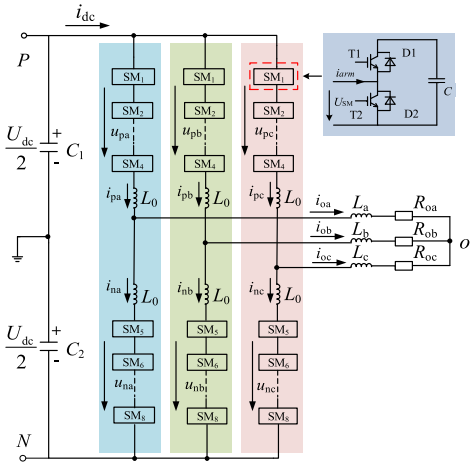

FIGURE 2. Topological diagram of a three-phase MMC. Where each phase contains many submodules with the same circuit topology.

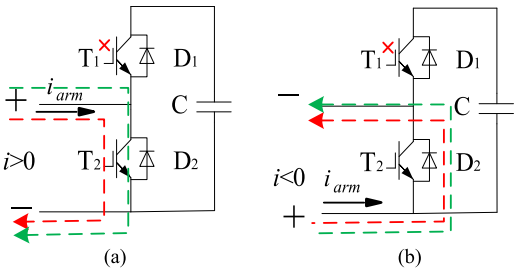

FIGURE 3. Current flow path of the SM under a T1 open-circuit fault with $S = 0$ (a), $i_{arm} > 0$ (b), $i_{arm} < 0$.

When an open-circuit fault occurs in an SM, T1 or T2 may be in either the on or off state. Different working states of SMs may exhibit different fault characteristics. Figures 3-6 show a comparison of the current flow paths before and after an open-circuit fault occurs in T1 or T2. The green dashed line represents the current path under normal conditions, while the red dashed line indicates the current path after a fault. When T1 experiences an open-circuit fault under $S = 0$, the capacitor of the faulty SM is in the cutoff state. Figure 3 shows that the open-circuit fault of T1 has no effect on the input or output current paths of the SM when $S = 0$.

In Figure 4, a T1 open-circuit fault occurs at $S = 1$, and the current direction of the SM affects the fault characteristics. If $i_{arm} > 0$, the T1 fault does not affect the current flow path of the SM. However, if $i_{arm} < 0$, the current will be forced to flow through the antiparallel diode D2, and the capacitor current of the SM will be 0. The SM capacitor lacks a discharge path, which signifies that means it can only be charged and cannot be discharged. Thus, the capacitor voltage of the SM will continue to increase.

Figure 5 shows that T2 exhibits an open-circuit fault at $S = 0$, and the current direction of the SM affects the fault characteristics. If $i_{arm} < 0$, the T2 fault does not influence the SM current path. However, if $i_{arm} > 0$, the current will be forced to flow through the antiparallel diode D1, and the

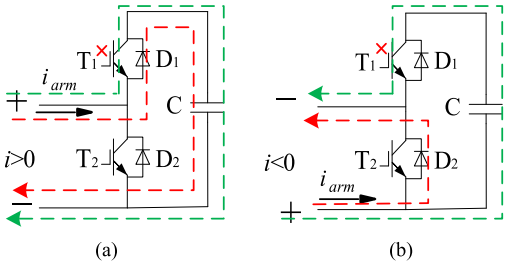

FIGURE 4. Current flow path of the SM under a T1 open-circuit fault with $S = 1$ (a), $i_{arm} > 0$ (b), $i_{arm} < 0$.

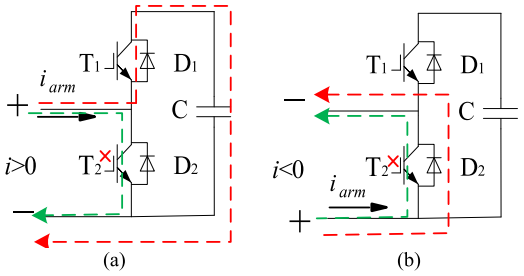

FIGURE 5. Current flow path of the SM under a T2 open-circuit fault with $S = 0$ (a), $i_{arm} > 0$ (b), $i_{arm} < 0$.

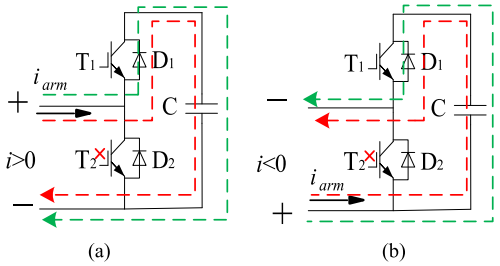

FIGURE 6. Current flow path of the SM under a T2 open-circuit fault with $S = 1$ (a), $i_{arm} > 0$ (b), $i_{arm} < 0$.

capacitor voltage of the SM will continue to rise. Figure 6 shows that the T2 open-circuit fault at $S = 1$ has no effect on the current direction of the SM.

In summary, the current and voltage of the SM after the occurrence of an open-circuit fault are shown in Table 1, which shows that the fault feature of a continuous voltage rise in the capacitor of the faulty SM can be used for fault location.

TABLE 1. Current and voltage of the SM after Occurrence of an open-circuit fault.

Fault type	i_{arm}	u_{SM}	u_{c} (SM capacitor voltage)
T1 open circuit	>0	u_{c}	normal
	<0	0	rise
	>0	0	normal
	<0	0	normal
T2 open circuit	>0	u_{c}	normal
	<0	u_{c}	normal
	>0	u_{c}	rise
	<0	0	normal

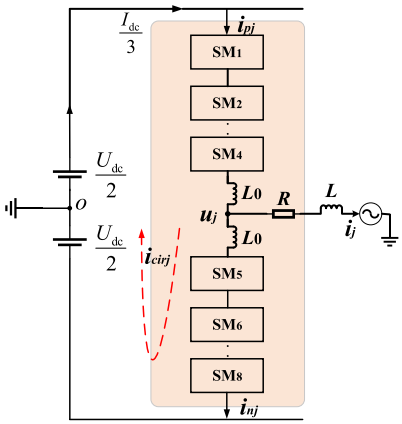

FIGURE 7. Single-phase equivalent circuit for the MMC topology diagram.

The structures of each bridge arm in the MMC are completely identical, and the voltage of each bridge arm cannot be completely constant in the steady operation state. There will be a circulating current in the upper and lower bridge arms. Therefore, the following discussion presents a specific analysis of the relationship between the bridge arm current and the circulating current. Without loss of generality, the equivalent circuit diagram of one phase of the MMC is used for analysis, as shown in Figure 7, where u_j (j = a,b,c) is the output voltage of the AC measurement, i_{pj} (j = a,b,c) is the upper bridge arm current, i_{nj} is the lower bridge arm current, I_{dc} is the DC current and O is the fictitious midpoint.

The following mathematical equations can be obtained by Kirchhoff's circuit laws:

$$i_{pj} = i_{cirj} + \frac{i_j}{2} \tag{2}$$

$$i_{nj} = i_{cirj} - \frac{i_j}{2} \tag{3}$$

where i_{cirj} is denoted as the circulating current and i_j (j = a,b,c) is the three-phase output current.

By subtracting (2) from (3), the equation of the output current can be derived as

$$i_j = i_{pj} - i_{nj} \tag{4}$$

By summing (2) and (3), the equation of the circulating current can be obtained as

$$i_{cirj} = \frac{i_{pj} + i_{nj}}{2} \tag{5}$$

The circulating current i_{cirj} consists of two parts: one part is the DC component with $I_{\text{dc}}/3$, and the other part is the AC component including the circulating current i_{dfn} caused by the three-phase voltage imbalance. It contains even harmonics that are mainly composed of 2, 4 and 6 frequency components.

The equations of the three-phase circulating currents can be expressed by

$$\begin{cases} i_{cira} = \dfrac{I_{dc}}{3} + \sum\limits_{n=2}^{\infty} I_{dfn}\cos(n\omega_0 t + \varphi_{dfn}) \\ i_{cirb} = \dfrac{I_{dc}}{3} + \sum\limits_{n=2}^{\infty} I_{dfn}\cos((n\omega_0 t - \dfrac{2}{3}\pi) + \varphi_{dfn}) \\ i_{circ} = \dfrac{I_{dc}}{3} + \sum\limits_{n=2}^{\infty} I_{dfn}\cos((n\omega_0 t + \dfrac{2}{3}\pi) + \varphi_{dfn}) \end{cases} \tag{6}$$

where I_{dc} is the DC-side current, I_{dfn} is the n times the circulation harmonic peak and φ_{dfn} is the initial phase.

The upper and lower arm currents of each phase include the AC component of the circulating current and the harmonic components. Therefore, when a T1 or T2 open-circuit fault occurs, the harmonic components in the circulating current will affect the output of the bridge arm current. Due to the inductance of the bridge arm, the bridge arm current i_{arm} can continue to flow. However, during the zero crossing of the forward current after the T1 fault and the zero crossing of the reverse current after the T2 fault, the i_{arm} is intermittent and fluctuates around the zero value, which prevents the circuit from normally generating the reverse current (T1 fault) or forward current (T2 fault). Moreover, the capacitor voltage of the faulty SM will continue to increase. Therefore, the fault characteristics of the intermittent bridge arm current after an open-circuit fault can be used to detect the faulty bridge arm within half a cycle time.

III. PROPOSED FAULT DETECTION AND LOCATION ALGORITHMS

To address the problem of fault diagnosis when an SM experiences an open circuit, an OCFD approach is proposed. Figure 8 shows the flowchart of the proposed hybrid machine learning method, which is divided into data processing, fault detection and fault localization steps.

A. THE PRINCIPLE OF QPSO-LSTM

The QPSO algorithm determines the optimal solution through collaboration and information sharing within a group [35], [39]. It is a widely used approach in optimization, neural network training, fuzzy system control and other application fields. The algorithm is improved on the basis of particle swarm optimization (PSO), which cancels the movement direction attribute of particles and increases the randomness of particle positions.

LSTM comprises forgetting gates, updating gates and output gates, as shown in Figure 9.

The entire process operation is called the forget gate, and the specific equation is expressed by (7):

$$f_t = \sigma(W_f \cdot [h_{t-1}, x_t] + b_f) \tag{7}$$

where W_f is the weight of the function, b_f represents the intercept of the function, the neural network output h_{t-1} at t-1 is combined with the input data x_{t-1} at t-1 for linear

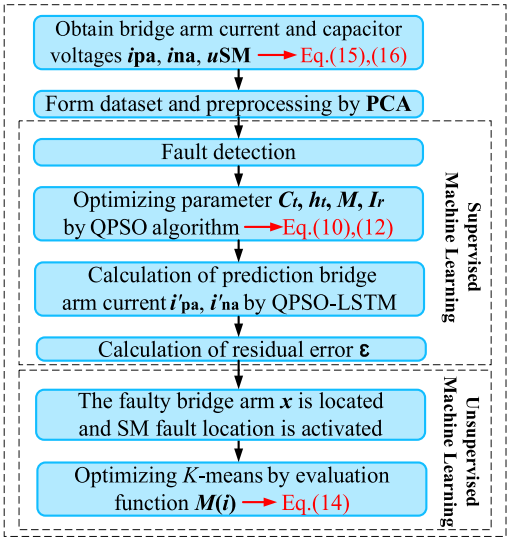

FIGURE 8. Flowchart of the proposed hybrid machine learning method for MMC diagnosis, which includes data processing, fault detection and fault localization.

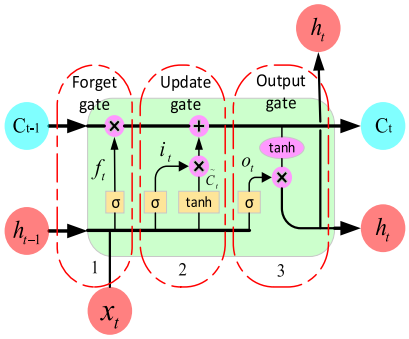

FIGURE 9. Architecture of the LSTM neural network model, which contains a forget gate, update gate and output gate.

transformation, and C_{t-1} is the unit state at the previous t-1 moment.

The gate updating process can be expressed as:

$$i_t = \sigma(W_i \cdot [h_{t-1}, x_t] + b_i) \tag{8}$$

$$\tilde{C}_t = \tanh(W_C \cdot [h_{t-1}, x_t] + b_C) \tag{9}$$

$$C_t = f_t * C_{t-1} + i_t * \tilde{C}_t \tag{10}$$

where W_i *and* W_C are the weights of the function and b_i and b_c represent the intercepts of the function.

The output gate is modeled using (11) and (12):

$$O_t = \sigma(W_o[h_{t-1}, x_t] + b_o) \tag{11}$$

$$h_t = o_t * \tanh(C_t) \tag{12}$$

where W_o *and* b_o are the weight of the function and the intercept of the function, respectively.

The QPSO algorithm is used to optimize four important parameters of the LSTM, including C_t in (10), h_t in (12), the number of iterations M, and the learning rate I_r.Figure 10

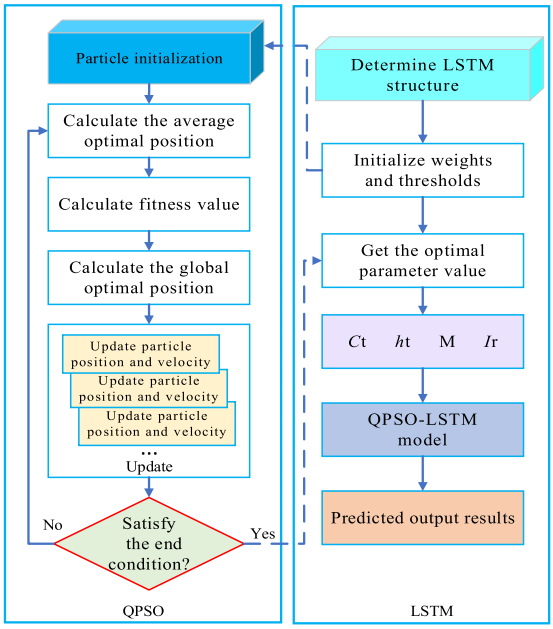

FIGURE 10. Architecture of the QPSO-LSTM neural network model, where Ct and *ht* represent the hidden layer, *M* is the number of iterations and *Ir* is the learning rate.

shows the framework of the QPSO-LSTM. The optimization of the LSTM using the QPSO algorithm includes two parts: the left side of the framework is the QPSO algorithm part, and the right side is the LSTM training part. The particle represents the weight and threshold in the LSTM. The prediction error calculated by the right network is taken as the particle fitness. The left and right parts are called back and forth, respectively, to iteratively find the optimal particle, this process is called the QPSO-LSTM algorithm.

Based on the above parameters, the learning rate I_r ranges from [0.0001, 0.01]. The QPSO algorithm is used to optimize the four parameters C_t, h_t, M and I_r of the LSTM. The fitness value of each particle is determined by the mean square error (*MSE*). The *MSE* is expressed by (13), where y_t is the real data and p_t is the predicted value:

$$MSE = \frac{1}{N}\sum_{t=1}^{N}(y_t - p_t)^2 \tag{13}$$

The *MSE* of the trained network and the optimization results of the QPSO algorithm are shown in Figure 11. Figure 11(a) shows that when the QPSO algorithm is iterated 20 times, the *MSE* of the trained network with respect to the optimization parameters is essentially stable, reaching a minimum error of approximately 0.042. Under these conditions, the number of neurons C_t in the first hidden layer equals 2, the number of neurons h_t in the second hidden layer approaches 178, the number of iterations M is 20, and the learning rate I_r changes with the number of iterations and is equal to 0.0014, as shown in Table 2. Therefore, the QPSO algorithm can optimize the four main parameters of the LSTM network in fewer iterations, as shown in Figure 11(b).

TABLE 2. Parameter values of the QPSO-LSTM neural network model.

Number of iterations	Fitness	Parameters value
5	0.055	*Ct*:100, *ht*:1, *M*:25, Ir:0.005
10	0.046	*Ct*:140, *ht*:180, *M*:25, Ir:0.005
15	0.043	*Ct*:100, *ht*:1, *M*:29, Ir:0.002
20	0.042	*Ct*:2, *ht*:178, *M*:20, Ir:0.0014

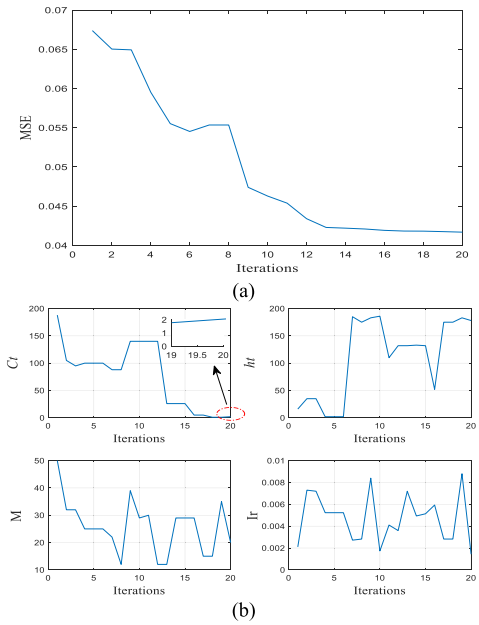

FIGURE 11. Parameter optimization of the LSTM neural network model by the QPSO algorithm (a), MSE of the trained network (b), parameters of the four optimized algorithms.

The proposed QPSO-LSTM fault detection algorithm is implemented in MATLAB 2021a on a personal computer (PC) with an Intel i5-9300(HQ) 2.4 GHz CPU and 8 GB of RAM. The QPSO-LSTM model is initialized with 200 hidden layers, a learning rate of 0.005 and 1000 iterations. One thousand samples are used as training data for each classification. Similarly, the Elman neural network, recurrent neural network (RNN), and radial basis function (RBF) neural network were constructed on the aforementioned dataset using MATLAB. Each algorithm is repeatedly tested 15 times, with five different test sets used each time. The corresponding results show that the QPSO-LSTM algorithm exhibits superior prediction ability, with the highest detection accuracy and fastest detection time among the five algorithms, as shown in Table 3.

TABLE 3. Comparison of different neural network algorithms.

Algorithms	Accuracy (%)	Detection Time (s)	Parameters
Elman	89.5	0.22	Hidden_sizes:15
RNN	96.3	0.12	Hidden_sizes: 5
RBF	87.5	0.092	Hidden_nums:10
PSO-LSTM	96.8	0.041	*Ct*:50, *ht*:150
QPSO-LSTM	98.7	0.035	*Ct*:2, *ht*:178

B. IMPROVED K-MEANS ALGORITHM

Considering the limitations of the K-means algorithm [40], [41] and combined with the characteristics of SMs after open-circuit faults, the main factor affecting data clustering is the selection of the K value. Therefore, a mixed evaluation function method is proposed to determine the K value in this paper. The mixed evaluation function method comprehensively considers the differences in cluster density and dispersion. Equation (14) defines the mixed evaluation function:

$$M(i) = \frac{b(i) - a(i)}{max(a(i), b(i))} \tag{14}$$

Equation (14) shows that the value range of the function is [−1,1], where $a(i)$ represents the average distance between sample i and other sample points in the same cluster. $b(i)$ reflects the average value of the distance between sample i and other nonclustered sample points. When $M(i)$ is close to 1, the distribution of sample i is reasonable.

C. HYBRID MACHINE LEARNING

The fault diagnosis method implemented in this paper adopts a hybrid machine learning approach, as shown in Figure 12. This hybrid approach comprises supervised machine learning and unsupervised machine learning. The QPSO-LSTM neural network is a supervised machine learning method that collects the bridge arm current as the input and is responsible for SM open-circuit fault detection. The QPSO-LSTM neural network needs to train the collected bridge arm current data, therefore, this algorithm is a type of supervised machine learning. Moreover, the K-means algorithm is an unsupervised machine learning algorithm that is used for SM open-circuit fault location. When an open-circuit fault is detected in the upper or lower bridge arm of a certain phase, the SM fault location is activated to collect and cluster the capacitor voltage data of all SMs on the faulty bridge arm. For the QPSO-LSTM neural network algorithm, the bridge arm data do not require much collection. However, this approach requires higher accuracy for fault detection. For SM fault location, supervised machine learning is not applicable because a large quantity of data needs to be collected. The K-means algorithm does not require training on sample data and can quickly locate faulty SMs, therefore, this algorithm is a type of unsupervised machine learning. Finally, by combining the advantages of both machine learning methods, hybrid machine learning methods have been developed.

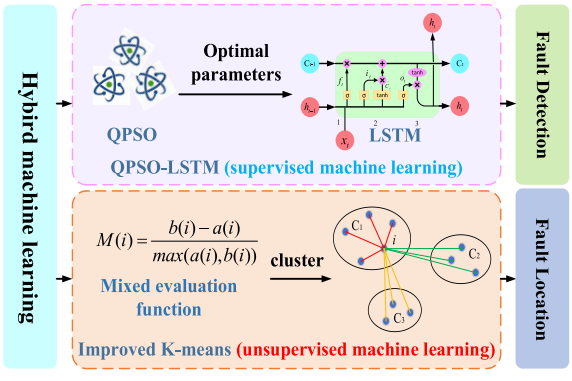

FIGURE 12. Framework of hybrid machine learning for MMC fault diagnosis, mainly includes supervised machine learning and unsupervised machine learning.

TABLE 4. Comparison with different fault diagnosis approaches.

Method	Method Category	OCFDL time	Accuracy	Empirical threshold	Multiple faults
[21]	Hardware	200μs	/	Yes	Yes
[22]	Hardware	<20ms	/	Yes	Yes
[23]	Hardware	≈1ms	/	Yes	Yes
[24]	Model	≈10ms	/	Yes	Yes
[25]	Model	<15ms	/	Yes	Yes
[26]	Model	<20ms	/	Yes	No
[27]	Model	≈40ms	/	Yes	No
[28]	Model	≈16ms	/	Yes	No
[29]	AI	≈20ms	99.2%	Yes	No
[31]	AI	≈150ms	/	Yes	Yes
[32]	AI	≈100ms	99.93%	No	No
[34]	AI	<20ms	98.4%	No	No
Proposed method	AI	<15ms	99.4%	No	Yes

D. COMPARISON WITH EXISTING OCFDL METHODS

To demonstrate the outstanding performance of the proposed OCFDL approach, several recently proposed methods for the MMC OCFDL are selected and compared with the proposed method, as shown in Table 4.

Generally, method [32] exhibits the highest accuracy, reaching 99.93%. The other methods listed in [29] and [34] exhibit lower accuracies than the proposed method, which exhibits 99.4% accuracy. In terms of the OCFL time, the proposed approach also achieves a faster OCFL speed (<15 ms) than do the other methods [22], [26], [27], [28], [29], [31], [32], [34]. The methods listed in [21], [22], [23], [24], [25], [26], [27], [28], [29], [30], and [31] rely on the manual setting of the empirical threshold. However, the thresholds change with the change in operation conditions of the MMC. Table 4 shows that several methods, such as [21], [22], [23], [24], [25], and [31], can handle multiple faults at the same time. The proposed approach is robust to external noise, does not require an empirical threshold and is suitable for multiple faults. This approach is a highlighted method.

IV. SIMULATION VERIFICATION AND ANALYSIS

To validate the effectiveness of the proposed data-driven method, a three-phase MMC system, as shown in Figure 2, is simulated in PSIM software. The OCFDL model was established using MATLAB and Jupyter notebook software. The simulation parameters are shown in Table 5.

TABLE 5. Parameters of simulation and experiment for the MMC prototype.

Parameter	Simulation	Experimental
DC-link voltage, U_{dc}	1 kV	80 V
Number of SMs per bridge arm, N	4	4
AC inductance, L_s	15 mH	5 mH
The bridge arm inductance, L_0	5 mH	3 mH
SM capacitance, C	2 mF	2 mF
Switching frequency, f_s	2 kHz	2 kHz
Operation frequency, f	50 Hz	50 Hz
Load resistance	10 Ω	10 Ω

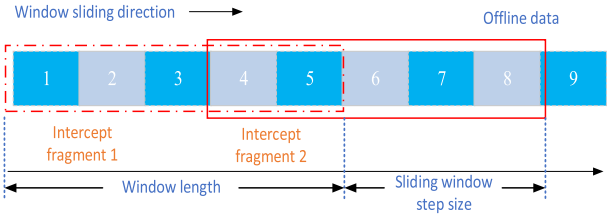

FIGURE 13. Schematic of the sliding window algorithm.

A. DATABASE BUILDING

The OCFDL method requires the use of a comprehensive database based on historical measurements or simulations. The characteristic values of six bridge arm currents in the normal working state are collected.

B. SLIDING WINDOW

In this paper, the voltage dataset of the SMs is characterized using statistics, with each SM voltage characterized by the maximum value $u_{\mathrm{SM-max}}$, minimum value $u_{\mathrm{SM-min}}$, root mean square value $u_{\mathrm{SM-rms}}$, and average value $u_{\mathrm{SM-avg}}$. The bridge arm current data need to be sampled. The sliding window method is used to segment the offline data and dynamically update the sampled voltage and current data. The offline data processing scheme is shown in Figure 13.

After off-line sampling and saving of the complete bridge arm current data, a window with a length of L_{win} is used to intercept the original information sequence with a length of L, and a data fragment with a length of L_{win} is obtained for each interception. Using sliding step segmentation, a new data fragment is obtained. The window continues to slide until the offline data have been fully segmented. If the number of remaining samples is less than the step size of the sliding window, then the window stops sliding.

The sliding window segmentation of each voltage sequence allows for the interception of all fragments of the original voltage sequence. The number of intercepted sliding windows S_{num} can be obtained by the window length L_{win}, the data length L, and the sliding window step L_{step}. The corresponding equation is as follows:

$$S_{\mathrm{num}} = \left\lfloor \frac{L - L_{win}}{L_{step}} \right\rfloor + 1 \tag{15}$$

$$\lfloor x \rfloor = \max \{ n \in Z \mid n \leq x \} \tag{16}$$

where, $\lfloor x \rfloor$ represents the largest integer not greater than x.

C. OFFLINE SIMULATION TEST AND ANALYSIS

To verify the effectiveness of the proposed fault diagnosis and location method, the SM capacitance and bridge arm inductance are adjusted by 5%, and 20 dB white Gaussian noise is added to the sampled signals. Considering the highly symmetrical structure of the three-phase MMC system, 20 sets of simulations are carried out. The sequence length is 100 ms (including 500 samples), the length of the sliding window during the fault detection stage is 20 ms, and the step size is 1 ms.

1) CASE 1 NORMAL OPERATION

The simulation results of the bridge arm current waveforms under normal operation conditions are shown in Figure 14(a), which are basically symmetrical and sinusoidal. The capacitance voltages of the SMs in phase A during normal operation are shown in Figure 14(b), and the capacitance voltage balancing effect is favorable and fluctuates approximately 250 V. Moreover, the QPSO-LSTM is used to predict the bridge arm current of phase A. The predicted results are essentially consistent with the recorded current, as shown in Figure 14(c), which indicates that the network has completed model training and has the ability to predict the bridge arm current. To evaluate the prediction accuracy of the various algorithms for the bridge arm current, the predicted current values of the LSTM, PSO-LSTM and QPSO-LSTM models are compared with the actual values, as shown in Figure 14(d). The figure shows that the current values predicted by the QPSO-LSTM model are closer to the experimental values.

2) CASE 2 SM1 OPEN-CIRCUIT FAULT AT 0.35 S

SM1 of the upper bridge arm in phase A is assumed to experience an open-circuit fault at 0.35 s. The faulty bridge arm current is shown in Figure 15(a). After the fault occurs, the bridge arm current is severely distorted, and the current tends to zero without a negative value. Moreover, the operation time is approximately 5 ms, and fault detection is completed. Figure 15(b) shows the capacitance voltages of the faulty bridge arm SMs, and it is clear that SM1 is far from SM2-SM4. As shown in Figure 15(c), the voltage of fault SM1 is clustered into one category, and the normal SMs are clustered into another category. In addition, the time is 10 ms, and the fault location is completed. The simulation results verify the effectiveness of the proposed fault diagnosis approach.

V. EXPERIMENTAL VERIFICATION AND ANALYSIS

To evaluate the effectiveness of the proposed fault diagnosis method, a downscaled three-phase MMC prototype with four SMs per arm was constructed in the laboratory. The experimental parameters are shown in Table 5. The configuration of the experimental setup is shown in Figure 16.

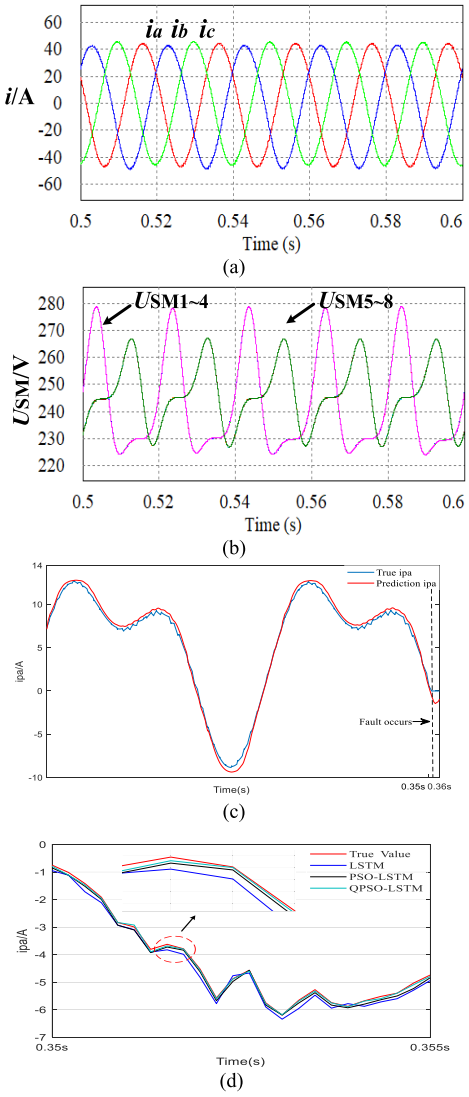

FIGURE 14. Output currents and voltages of the 5-level MMC under normal conditions in simulation (a), three-phase output currents (b), output capacitor voltages of the SMs in A-phase (c), actual values and predicted values of the A-phase bridge arm current (d), predicted values of the A-phase bridge arm current under different algorithms and actual values.

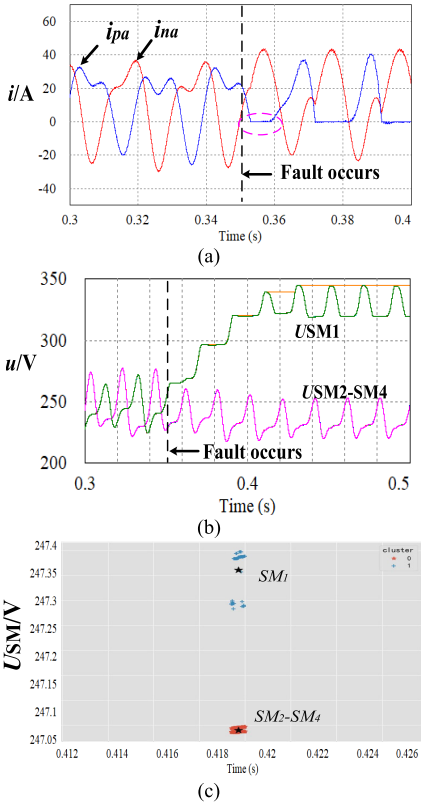

FIGURE 15. Output currents and voltages of the 5-level MMCs under an open-circuit fault in simulation (a), output current of the A-phase bridge arm (b), output capacitor voltages of the SMs in the A-phase, and (c) fault localization of SM1.

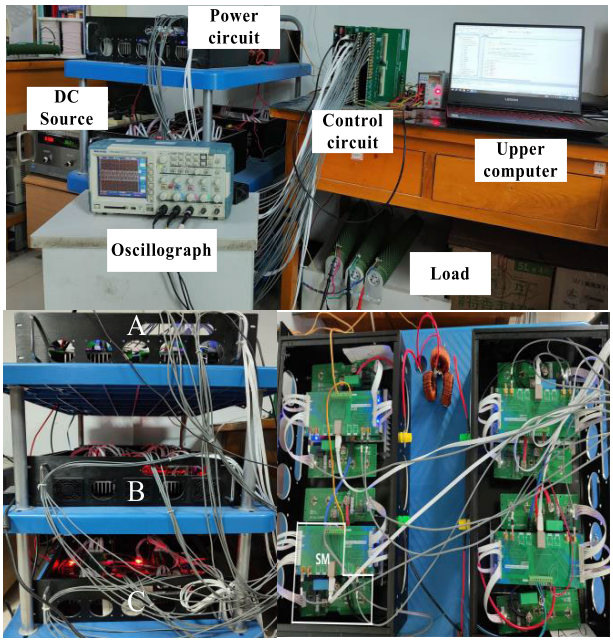

FIGURE 16. Experimental platform of the three-phase MMC prototype, mainly includes the experimental platform, main circuit and SMs of one phase.

All the data acquisition, data processing, and PWM generation steps are implemented by an ARM (STM32H750IBK6) and an FPGA (EP4CE10F17C8N). The ARM is mainly responsible for the control algorithm and data processing, while the FPGA is responsible for PWM generation, capacitance voltage equalization and other functions. The two are coordinated and operated through SPI communication. In the experiment, an IGBT open-circuit fault is simulated by blocking the corresponding gate drive signal. Finally, all the experimental data are transmitted to the upper computer for fault diagnosis.

A. NORMAL OPERATION

Figure 17 shows the experimental results of the three-phase MMC system during normal operation. Figure 17(a) shows that the three-phase voltages are essentially symmetrical and sinusoidal. However, the waveform of ua clearly decreases when the SM fails. Therefore, the performance of the MMC

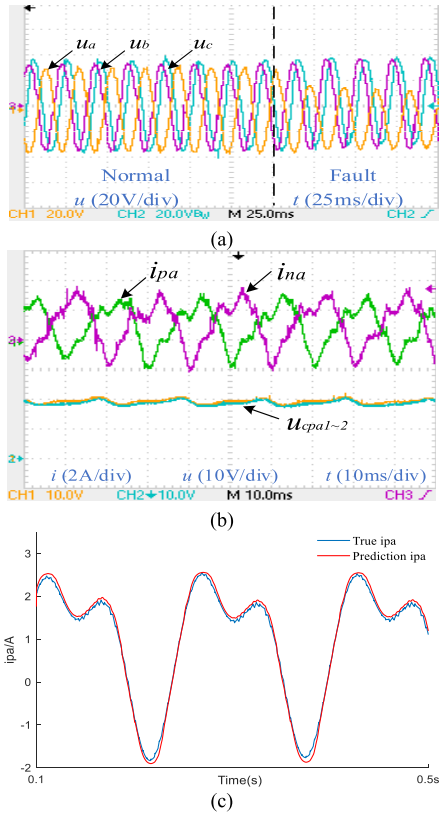

FIGURE 17. Experimental results of the 5-level MMC under normal case (a), three-phase output voltages. (b), waveforms of bridge arm currents and SM capacitor voltages in A-phase. (c), waveforms of predicted i_{pa} and actual bridge arm currents in normal state.

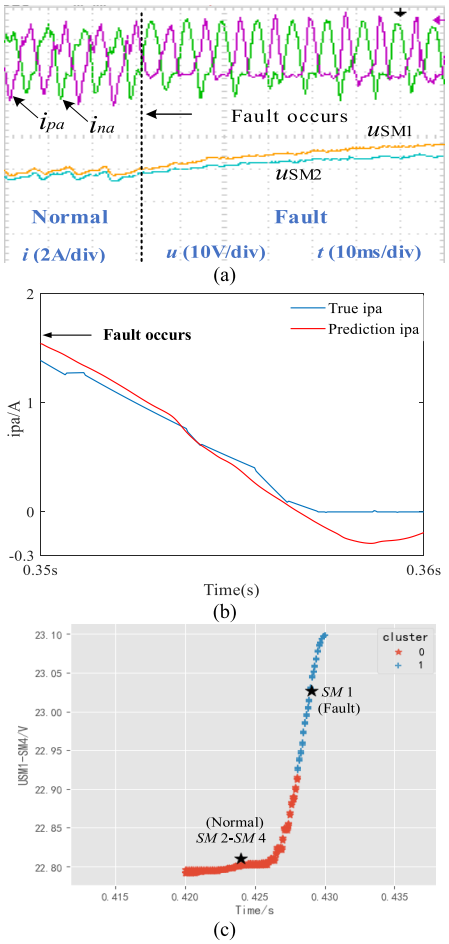

FIGURE 18. Experimental results of the 5-level MMC under the SM1 T1 open-circuit fault case at 0.35 s (a), waveforms of bridge arm currents and SM capacitor voltages in A-phase (b), fault detection result of SM1 (c), fault localization result of SM1.

system degrades. Figure 17(b) shows the bridge arm currents and the capacitance voltages of the two SMs for phase A. Figure 17(b) shows that the capacitance voltages of the SMs are essentially the same, fluctuating at approximately 20 V. The currents of the upper and lower bridge arms vary positively and negatively, respectively, under normal conditions and contain harmonics. Figure 17(c) shows the i_{pa} waveforms of the predicted and actual bridge arm currents in the normal state. The predicted bridge arm current is basically consistent with the actual current, indicating that the QPSO-LSTM model is accurate.

B. T1 FAULTS IN THE SM1

Figure 18(a) shows the changes in the bridge arm currents and SM capacitor voltages before and after the T1 open-circuit fault of SM1 of the upper bridge arm on the phase A. After the fault occurs, the capacitor voltages of the SMs increase synchronously. Clearly, the rate of increase in the capacitance voltage of the faulty SM is significantly greater than that of the healthy SM. The upper bridge arm current *i*pa has no negative value, and the minimum current of the bridge arm is basically zero due to reverse blocking of the freewheeling diode when a fault occurs.

The current i_{na} has little effect, and the capacitor of each SM of the lower bridge arm can still be charged and discharged normally. After a period, the capacitor voltage of the faulty SM deviates from that of the normal SM. The T1 fault detection result for SM1 is shown in Figure 18(b). The error between the predicted current i_{pa} and the true value of the bridge arm is greater than the set threshold. Moreover, as the residual value increases, it almost reaches 0.3 A at 0.36 s, and the fault detection time is 10 ms. To prevent the system from mislocating, the location duration is extended by 3 cycles (60 ms) to make the distinction between the faulty and the normal SMs clearer. Therefore, the system detects the faulty bridge arm and activates the fault isolation mechanism.

The fault location results are shown in Figure 18(c). The capacitor voltages of the normal and fault SMs increase almost synchronously. The improved K-means clustering algorithm divides the data into two categories, and the result of the SM1 value being far from those of SM2-SM4 indicates that SM1 has an open-circuit fault. The above analysis reveals that T1 of SM1 has an open-circuit fault.

C. T2 FAULTS IN THE SM5

The time to complete the fault detection and location is approximately 80 ms. Similarly, Figure 19(a) shows the changes in bridge arm currents and SM capacitor voltages

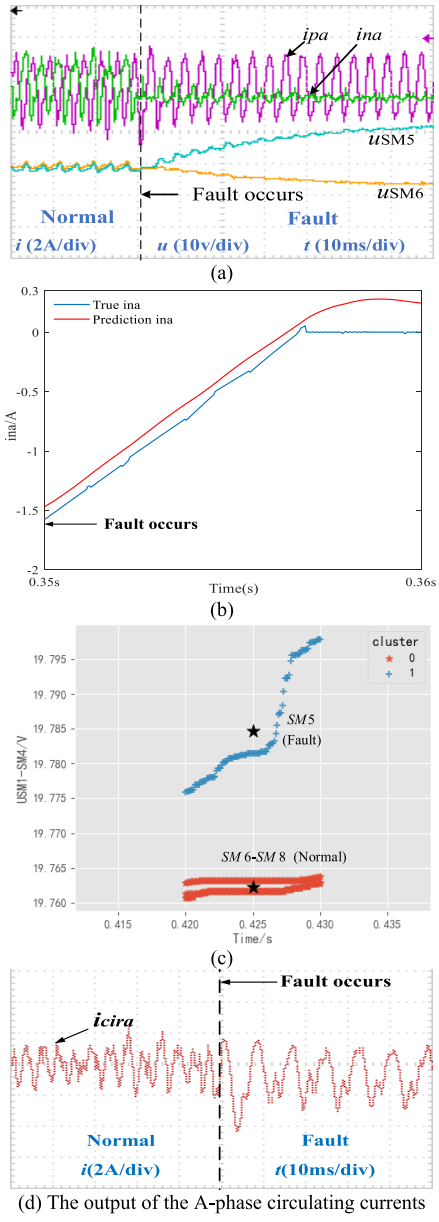

FIGURE 19. Experimental results of the 5-level MMC under the SM5 T2 open-circuit fault case at 0.35 s (a), waveforms of bridge arm currents and SM capacitor voltages in A-phase (b), fault detection result of SM5 (c), fault localization result of the SM5 (d), output of the A-phase circulating currents.

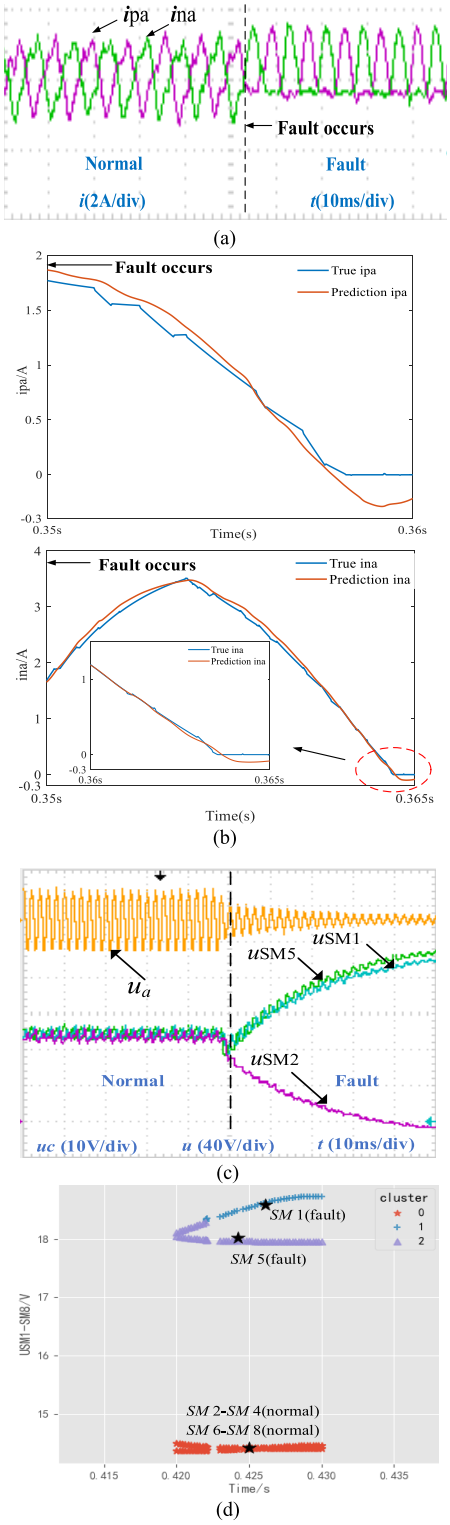

FIGURE 20. Experimental results of the 5-level MMC under the SM1 T2 and SM5 T2 simultaneously open-circuit fault cases at 0.35 s (a), waveforms of bridge arm currents in A-phase (b), fault detection results of SM1 and SM5 (c), waveforms of SM capacitor voltages in A-phase (d), fault localization results of SM1 and SM5.

before and after the T2 open-circuit fault of SM5 of the lower bridge arm in phase A. As shown, the amplitude of the bridge arm current i_{na} decreases, the capacitor voltage of the fault SM increases, the capacitor voltages of the normal SMs decrease, and the difference is clear. The T2 fault detection result for SM5 is shown in Figure 19(b). The fault location results are shown in Figure 19(c). The data are divided into two categories, which are consistent with the theoretical analysis. The fault detection and location results are the same as those for the set position, and the time needed to complete the fault detection and location is approximately 80 ms. Figure 19(d) shows that the waveform for the circulating current and the vibration of the waveform intensify when the fault occurs.

D. T2 SYNCHRONOUSLY FAULTS IN SM1 AND SM5

Figure 20(a) shows the changes in bridge arm currents before and after the open-circuit fault of SM1 and SM5 in phase A. There is no negative phase current on the upper bridge arm or the lower bridge arm when the fault occurs. Figure 20(b) shows the fault detection results for SM1 and SM5. The error between the true and predicted values of i_{pa} increases, reaching almost 0.3 A at 0.36 s, and the fault detection time is 10 ms. i_{na} has little impact on the fault. After a period, the error between the true and predicted values of i_{na} also increases, reaching almost 0.3 A at 0.365 s. Figure 20(c) shows that the capacitor voltages of SM1 of the upper bridge arm and SM5 of the lower bridge arm increase, and the residual SM capacitor voltage decreases, which is consistent with the theoretical analysis.

Figure 20(d) shows that the improved K-means clustering algorithm can accurately and quickly distinguish fault SMs from healthy SMs. A large amount of data show that this method can accurately detect and locate different open-circuit faults, such as open-circuit faults of one SM, multiple SMs of the same bridge arm, SMs of upper and lower bridge arms for a single phase, and similar open-circuit faults between phases, moreover, the total time for fault diagnosis and location is nearly 80 ms.

VI. CONCLUSION

The MMC system has low reliability due to the large number of SMs. The problems of detecting and locating open-circuit faults in SMs are studied in this paper. The sampled bridge arm current and the capacitor voltage of each SM are collected by the sliding window algorithm. The QPSO method is used to optimize several key parameters of the LSTM neural network to achieve the optimal balance between diagnostic accuracy and diagnostic speed. The proposed QPSO-LSTM method can predict the current of a bridge arm and accurately detect open-circuit faults in SMs, with a prediction accuracy of 98.69%. The improved K-means clustering algorithm can quickly locate faulty SMs, and the total time for fault diagnosis under various open-circuit fault conditions is close to 80 ms. In addition, accurate mathematical models are not needed, preventing the collection of fault samples. The simulation and experimental results demonstrate the effectiveness of the proposed OCFDL scheme, which has favorable application value for fault diagnosis of complex MMC systems.

REFERENCES

[1] J. Zhang, X. Hu, S. Xu, Y. Zhang, and Z. Chen, "Fault diagnosis and monitoring of modular multilevel converter with fast response of voltage sensors," *IEEE Trans. Ind. Electron.*, vol. 67, no. 6, pp. 5071–5080, Jun. 2020, doi: 10.1109/TIE.2019.2928248.

[2] H. Li, X. Fan, and S. Liu, "Small-signal stability modeling for MMC-based DC grids with voltage slope control and influence analysis of parameters," *IEEE Access*, vol. 10, pp. 4686–4698, 2022, doi: 10.1109/ACCESS.2021.3138739.

[3] B. Li, S. Shi, B. Wang, G. Wang, W. Wang, and D. Xu, "Fault diagnosis and tolerant control of single IGBT open-circuit failure in modular multilevel converters," *IEEE Trans. Power Electron.*, vol. 31, no. 4, pp. 3165–3176, Apr. 2016.

[4] Y. Xu, Z. Zhang, G. Wang, and Z. Xu, "Modular multilevel converter with embedded energy storage for bidirectional fault isolation," *IEEE Trans. Power Del.*, vol. 37, no. 1, pp. 105–115, Feb. 2022, doi: 10.1109/TPWRD.2021.3054022.

[5] X. Shi, S. Filizadeh, and A. Gole, "Capacitor energy storage requirements in mixed-submodule hybrid cascaded MMCs," *IEEE Trans. Energy Convers.*, vol. 35, no. 3, pp. 1638–1647, Sep. 2020, doi: 10.1109/TEC.2020.2987766.

[6] A. Lachichi, A. Junyent-Ferre, and T. C. Green, "Comparative optimization design of a modular multilevel converter tapping cells and a 2L-VSC for hybrid LV AC/DC microgrids," *IEEE Trans. Ind. Appl.*, vol. 55, no. 3, pp. 3228–3240, May 2019, doi: 10.1109/TIA.2019.2897263.

[7] S. Yang, J. Fang, Y. Tang, H. Qiu, C. Dong, and P. Wang, "Modular multilevel converter synthetic inertia-based frequency support for medium-voltage microgrids," *IEEE Trans. Ind. Electron.*, vol. 66, no. 11, pp. 8992–9002, Nov. 2019, doi: 10.1109/TIE.2018.2890491.

[8] D. Ma, W. Chen, L. Shu, X. Qu, and K. Hou, "A MMC-based multiport power electronic transformer with shared medium-frequency transformer," *IEEE Trans. Circuits Syst. II, Exp. Briefs*, vol. 68, no. 2, pp. 727–731, Feb. 2021, doi: 10.1109/TCSII.2020.3012293.

[9] B. Fan, Y. Li, K. Wang, Z. Zheng, and L. Xu, "Hierarchical system design and control of an MMC-based power-electronic transformer," *IEEE Trans. Ind. Informat.*, vol. 13, no. 1, pp. 238–247, Feb. 2017, doi: 10.1109/TII.2016.2522190.

[10] S. Nakamura and H. Yamada, "Single-phase grid-tied modular multilevel converter for various renewable energy sources," in *Proc. 24th Int. Conf. Electr. Mach. Syst. (ICEMS)*, Oct. 2021, pp. 281–285.

[11] S. Du, B. Wu, K. Tian, N. R. Zargari, and Z. Cheng, "An active cross-connected modular multilevel converter (AC-MMC) for a medium-voltage motor drive," *IEEE Trans. Ind. Electron.*, vol. 63, no. 8, pp. 4707–4717, Aug. 2016, doi: 10.1109/TIE.2016.2547875.

[12] D. Ronanki and S. S. Williamson, "Modular multilevel converters for transportation electrification: Challenges and opportunities," *IEEE Trans. Transport. Electrific.*, vol. 4, no. 2, pp. 399–407, Jun. 2018, doi: 10.1109/TTE.2018.2792330.

[13] J. Mei, P. Zhu, L. Yan, G. Fan, R. Ge, and B. Wang, "An enhanced modular multilevel converter with flexible interruption capability of DC-side fault," *IEEE Access*, vol. 7, pp. 156500–156512, 2019, doi: 10.1109/ACCESS.2019.2945965.

[14] X. Xiao, W. Su, J. Zhang, J. Yang, X. Si, X. Zhang, and J. Guo, "Comparison of grounding modes of MMC-based flexible DC distribution network," in *Proc. IEEE 4th Conf. Energy Internet Energy Syst. Integr. (EI2)*, Wuhan, China, Oct. 2020, pp. 2914–2919.

[15] S. Yang, A. Bryant, P. Mawby, D. Xiang, L. Ran, and P. Tavner, "An industry-based survey of reliability in power electronic converters," *IEEE Trans. Ind. Appl.*, vol. 47, no. 3, pp. 1441–1451, May 2011, doi: 10.1109/TIA.2011.2124436.

[16] S. Gao, H. Ye, and Y. Liu, "Accurate and efficient estimation of short-circuit current for MTDC grids considering MMC control," *IEEE Trans. Power Del.*, vol. 35, no. 3, pp. 1541–1552, Jun. 2020, doi: 10.1109/TPWRD.2019.2946603.

[17] U.-M. Choi, F. Blaabjerg, and K.-B. Lee, "Study and handling methods of power IGBT module failures in power electronic converter systems," *IEEE Trans. Power Electron.*, vol. 30, no. 5, pp. 2517–2533, May 2015, doi: 10.1109/TPEL.2014.2373390.

[18] K. Song, "Research on intelligent fault diagnosis technology of power electronic circuits," in *Proc. Int. Conf. Control Sci. Electric Power Syst. (CSEPS)*, Shanghai, China, May 2021, pp. 291–294.

[19] T. Soong and P. W. Lehn, "Assessment of fault tolerance in modular multilevel converters with integrated energy storage," *IEEE Trans. Power Electron.*, vol. 31, no. 6, pp. 4085–4095, Jun. 2016, doi: 10.1109/TPEL.2015.2477834.

[20] Q. Zhang, D. Xie, Y. Lei, and X. Ge, "A fast open-circuit fault diagnosis method for two-level converter in railway traction systems," in *Proc. IEEE 12th Energy Convers. Congr. Expo. Asia (ECCE-Asia)*, May 2021, pp. 2046–2051.

[21] X. Chen, J. Liu, Z. Deng, S. Song, S. Du, and D. Wang, "A diagnosis strategy for multiple IGBT open-circuit faults of modular multilevel converters," *IEEE Trans. Power Electron.*, vol. 36, no. 1, pp. 191–203, Jan. 2021, doi: 10.1109/TPEL.2020.2997963.

[22] J. Wang, H. Ma, and Z. Bai, "A submodule fault ride-through strategy for modular multilevel converters with nearest level modulation," *IEEE Trans. Power Electron.*, vol. 33, no. 2, pp. 1597–1608, Feb. 2018, doi: 10.1109/TPEL.2017.2679439.

[23] M. R. Haredasht, S. M. Barakati, S. Y. Darmian, M. B. Hashkavayi, and V. Barahouei, "Open-circuit fault diagnosis strategy for modular multilevel converter semiconductor power switches," in *Proc. 13th Power Electron., Drive Syst., Technol. Conf. (PEDSTC)*, Tehran, Iran, Feb. 2022, pp. 150–154, doi: 10.1109/PEDSTC53976.2022.9767349.
[24] L. Wang, L. Zhang, Y. Xiong, and Z. Kang, "Multi-point open circuit faults diagnosis strategy of modular multilevel converter under low modulation index," *IEEE Trans. Ind. Electron.*, vol. 71, no. 7, pp. 7886–7895, Jul. 2024, doi: 10.1109/TIE.2023.3306404.
[25] H. Jia, Y. Deng, X. Hu, Z. Deng, and X. He, "A concurrent diagnosis method of IGBT open-circuit faults in modular multilevel converters," *IEEE J. Emerg. Sel. Topics Power Electron.*, vol. 11, no. 1, pp. 1021–1034, Feb. 2023.
[26] Z. Wang and L. Peng, "Grouping capacitor voltage estimation and fault diagnosis with capacitance self-updating in modular multilevel converters," *IEEE Trans. Power Electron.*, vol. 36, no. 2, pp. 1532–1543, Feb. 2021, doi: 10.1109/TPEL.2020.3011131.
[27] D. Zhou, H. Qiu, S. Yang, and Y. Tang, "Submodule voltage similarity-based open-circuit fault diagnosis for modular multilevel converters," *IEEE Trans. Power Electron.*, vol. 34, no. 8, pp. 8008–8016, Aug. 2019, doi: 10.1109/TPEL.2018.2883989.
[28] H. Wu, Y. Wang, Y. Liu, R. Li, P. Li, and Y. Xue, "A threshold adaptive open-circuit submodule fault diagnosis strategy for modular multilevel converters," in *Proc. IEEE Int. Power Electron. Appl. Conf. Expo. (PEAC)*, Guangdong, China, Nov. 2022, pp. 1206–1210, doi: 10.1109/PEAC56338.2022.9959650.
[29] X. Hu, H. Jia, and Y. Deng, "An open circuit faults diagnosis method based on XG-boost used in MMC," in *Proc. Int. Conf. Power Syst. Technol. (POWERCON)*, Haikou, China, Dec. 2021, pp. 1805–1810.
[30] X. Hu, H. Jia, Y. Zhang, and Y. Deng, "An open-circuit faults diagnosis method for MMC based on extreme gradient boosting," *IEEE Trans. Ind. Electron.*, vol. 70, no. 6, pp. 6239–6249, Jun. 2023, doi: 10.1109/TIE.2022.3194584.
[31] Q. Yang, J. Qin, and M. Saeedifard, "Analysis, detection, and location of open-switch submodule failures in a modular multilevel converter," *IEEE Trans. Power Del.*, vol. 31, no. 1, pp. 155–164, Feb. 2016, doi: 10.1109/TPWRD.2015.2477476.
[32] S. Kiranyaz, A. Gastli, L. Ben-Brahim, N. Al-Emadi, and M. Gabbouj, "Real-time fault detection and identification for MMC using 1-D convolutional neural networks," *IEEE Trans. Ind. Electron.*, vol. 66, no. 11, pp. 8760–8771, Nov. 2019, doi: 10.1109/TIE.2018.2833045.
[33] Z. Bai, Y. Guo, S. Jiang, and L. Kong, "Fault diagnosis and location approach of modular multilevel converter based on dual one-dimensional convolutional neural network," in *Proc. IEEE Transp. Electrific. Conf. Expo., Asia–Pacific (ITEC Asia–Pacific)*, Haining, China, Oct. 2022, pp. 1–5, doi: 10.1109/ITECAsia-Pacific56316.2022.9941818.
[34] L. Ke, G. Hu, Y. Yang, and Y. Liu, "Fault diagnosis for modular multilevel converter switching devices via multimodal attention fusion," *IEEE Access*, vol. 11, pp. 135035–135048, 2023, doi: 10.1109/ACCESS.2023.3336953.
[35] Y. Han, W. Qi, N. Ding, and Z. Geng, "Short-time wavelet entropy integrating improved LSTM for fault diagnosis of modular multilevel converter," *IEEE Trans. Cybern.*, vol. 52, no. 8, pp. 7504–7512, Aug. 2022.
[36] L. Ke, Y. Liu, and Y. Yang, "Compound fault diagnosis method of modular multilevel converter based on improved capsule network," *IEEE Access*, vol. 10, pp. 41201–41214, 2022.
[37] L. Tong, Y. Chen, T. Xu, and Y. Kang, "Fault diagnosis for modular multilevel converter (MMC) based on deep learning: An edge implementation using binary neural network," *IEEE J. Emerg. Sel. Topics Power Electron.*, vol. 11, no. 6, pp. 5553–5568, Dec. 2023.
[38] Z. Wang, Y. Li, and X. Yin, "Visual MMC open circuit fault real-time rapid detection system," *IEEE Access*, vol. 11, pp. 15030–15037, 2023.
[39] W. Kong, Z. Y. Dong, Y. Jia, D. J. Hill, Y. Xu, and Y. Zhang, "Short-term residential load forecasting based on LSTM recurrent neural network," *IEEE Trans. Smart Grid*, vol. 10, no. 1, pp. 841–851, Jan. 2019, doi: 10.1109/TSG.2017.2753802.
[40] F. Moodi and H. Saadatfar, "An improved K-means algorithm for big data," *IET Softw.*, vol. 16, no. 1, pp. 48–59, Jun. 2021, doi: 10.1049/sfw2.12032.
[41] A. K. Maddirala and K. C. Veluvolu, "SSA with CWT and k-means for eye-blink artifact removal from single-channel EEG signals," *Sensors*, vol. 22, no. 3, p. 931, Jan. 2022, doi: 10.3390/s22030931.

YANG AN was born in Xi'an, China, in 1990. He received the B.S. degree in electrical engineering from Xi'an Technology of University, in 2015, and the M.S. degree in electrical and information engineering from Lanzhou University of Technology, in 2019. He is currently pursuing the Ph.D. degree with Xi'an University of Technology. His research interests include MMC fault diagnosis and location, fault-tolerant control, and life prediction based on artificial intelligence.

XIANGDONG SUN (Member, IEEE) was born in Shenyang, China, in 1971. He received the Ph.D. degree in electrical engineering from Xi'an University of Technology, Xi'an, China, in 2003. He did a postdoctoral research with Tokyo Polytechnic University supported by the Government Scholarship of Japan, from 2006 to 2008. Since 2009, he has been with the Department of Electrical Engineering, Xi'an University of Technology. His research interests include motor control, power electronics, and renewable energy systems.

BIYING REN was born in Henan, China, in 1971. She received the B.Sc., M.Sc., and Ph.D. degrees in electrical engineering from Xi'an University of Technology, Xi'an, China, in 1995, 2001, and 2009, respectively. Since 1998, she has been with the Department of Electrical Engineering, Xi'an University of Technology, where she is currently an Associate Professor. Her research interests include renewable energy systems and microgrid operation systems.

XIAOBIN ZHANG (Member, IEEE) was born in Shanxi, China, in 1977. He was a Senior Member of China Power Supply Society and a member of China Electrical Engineering Society. He was also a Visiting Scholar with Texas A&M University and Tsinghua University, USA. His research interests include new energy grid control, system stability analysis and optimization scheduling of microgrids, power quality control of distribution networks, modeling and control of power converters, bidirectional converters, and grid converters for renewable energy systems.